

Extreme Broadband Transparent Optical Phase Change Materials for High-Performance Nonvolatile Photonics

Yifei Zhang^{1†}, Jeffrey B. Chou^{2†*}, Junying Li^{3†}, Huashan Li^{4†}, Qingyang Du¹, Anupama Yadav⁵, Si Zhou⁶, Mikhail Y. Shalaginov¹, Zhuoran Fang¹, Huikai Zhong¹, Christopher Roberts², Paul Robinson², Bridget Bohlin², Carlos R ís¹, Hongtao Lin⁷, Myungkoo Kang⁵, Tian Gu¹, Jamie Warner⁶, Vladimir Liberman², Kathleen Richardson⁵, Juejun Hu^{1,*}

¹*Department of Materials Science & Engineering, Massachusetts Institute of Technology, Cambridge, Massachusetts, USA*

²*Lincoln Laboratory, Massachusetts Institute of Technology, Lexington, Massachusetts, USA*

³*Shanghai Key Laboratory of Modern Optical Systems, College of Optical-Electrical and Computer Engineering, University of Shanghai for Science and Technology, Shanghai, China*

⁴*Sino-French Institute for Nuclear Energy and Technology, Sun Yat-sen University, Guangzhou, China*

⁵*The College of Optics & Photonics, Department of Materials Science and Engineering, University of Central Florida, Orlando, USA*

⁶*Department of Materials, University of Oxford, Oxford, U.K.*

⁷*College of Information Science & Electronic Engineering, Zhejiang University, Hangzhou, China*

† These authors contributed equally to this work.

*jeff.chou@ll.mit.edu, hujuejun@mit.edu

Abstract

Optical phase change materials (O-PCMs), a unique group of materials featuring drastic optical property contrast upon solid-state phase transition, have found widespread adoption in photonic switches and routers, reconfigurable meta-optics, reflective display, and optical neuromorphic computers. Current phase change materials, such as Ge-Sb-Te (GST), exhibit large contrast of both refractive index (Δn) and optical loss (Δk), simultaneously. The coupling of both optical properties fundamentally limits the function and performance of many potential applications. In this article, we introduce a new class of O-PCMs, Ge-Sb-Se-Te (GSST) which breaks this traditional coupling, as demonstrated with an optical figure of merit improvement of more than two orders of magnitude. The first-principle computationally optimized alloy, $\text{Ge}_2\text{Sb}_2\text{Se}_4\text{Te}_1$, combines broadband low loss ($1 - 18.5 \mu\text{m}$), large optical contrast ($\Delta n = 2.0$), and significantly improved glass forming ability, enabling an entirely new field of infrared and thermal photonic devices. We further leverage the material to demonstrate nonvolatile integrated optical switches with record low loss and large contrast ratio, as well as an electrically addressed, microsecond switched pixel level spatial light modulator, thereby validating its promise as a platform material for scalable nonvolatile photonics.

DISTRIBUTION STATEMENT A. Approved for public release. Distribution is unlimited.

This material is based upon work supported by the Assistant Secretary of Defense for Research and Engineering under Air Force Contract No. FA8702-15-D-0001. Any opinions, findings, conclusions or recommendations expressed in this material are those of the author(s) and do not necessarily reflect the views of the Assistant Secretary of Defense for Research and Engineering.

© 2018 Massachusetts Institute of Technology

Delivered to the U.S. Government with Unlimited Rights, as defined in DFARS Part 252.227-7013 or 7014 (Feb 2014). Notwithstanding any copyright notice, U.S. Government rights in this work are defined by DFARS 252.227-7013 or DFARS 252.227-7014 as detailed above. Use of this work other than as specifically authorized by the U.S. Government may violate any copyrights that exist in this work.

When O-PCMs undergo solid-state phase transition, their optical properties are significantly altered. This singular behavior, identified in a handful of complex oxides^{1,2} as well as chalcogenide alloys exemplified by the GST family^{3,4}, has been exploited in a wide range of photonic devices including optical switches⁵⁻¹⁰, nonvolatile display¹¹, reconfigurable meta-optics¹²⁻¹⁷, tunable emitters and absorbers¹⁸⁻²⁰, photonic memories^{21,22}, and all-optical computers²³. To date, these devices only leverage phase change materials originally developed for electronic switching. Optical property modulation in these classical phase change material systems stems from metal-insulator transitions (MIT) accompanying structural transformations²⁴. The introduction of large amounts of free carriers in the metallic or conductive state, while essential to conferring conductivity contrast for electronic applications, results in excessive loss increase due to free carrier absorption (FCA). The concurrent index and loss changes fundamentally limits the scope of their potential optical applications. Breaking such coupling allows independent control of the phase and amplitude of light waves, a Holy Grail for optical engineers that opens up numerous applications including ultra-compact and low-loss modulators²⁵, tunable thermal emission²⁶ and radiative cooling²⁷, beam steering using phase-only modulation²⁸, and large-scale photonic deep neural network²⁹. Decoupling of the two effects is customarily characterized using the material figure-of-merit (FOM), expressed as:

$$\text{FOM} = \frac{\Delta n}{\Delta k}, \quad (1)$$

where Δn and Δk denote the real and imaginary parts of refractive index change induced by the phase transition, respectively. It has been shown that this generic FOM quantitatively correlates with the performance of many different classes of photonic devices³⁰⁻³³. Current O-PCMs such as GST and the classical Mott insulator VO₂ suffer from poor FOM's in the order of unity, imposing a major hurdle towards their optical applications.

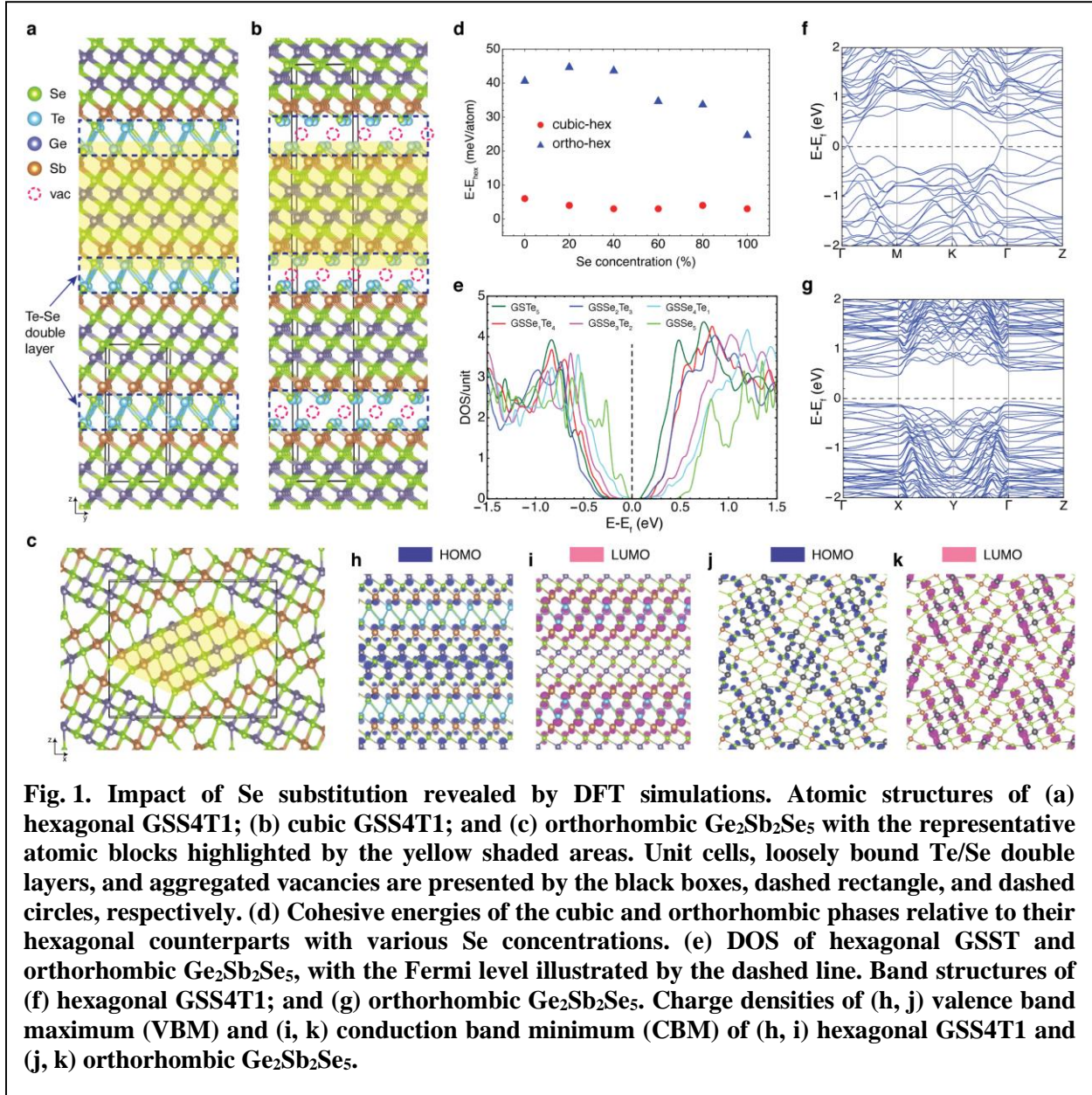
Besides the low FOM, limited switching volume poses an additional challenge for existing chalcogenide O-PCMs. The poor amorphous phase stability of GST mandates a high cooling rate in the order of 10¹⁰ °C/s to ensure full re-amorphization during melt quenching³⁴, which coupled with their low thermal conductivity³⁵ stipulates a film thickness of around 150 nm or less if complete, reversible switching is to be achieved. While not an issue for today's deeply-scaled electronic memories, it constrains optical devices to thin film designs.

In this article, we report an O-PCM Ge-Sb-Se-Te (GSST) with unprecedented broadband optical transparency and exceptionally large FOM throughout almost the entire infrared spectrum. The material therefore represents a new class of O-PCMs where the phase transition *only* triggers refractive index modulation but without the loss penalty. While Se doping in phase change alloys has been previously investigated³⁶⁻⁴⁰, such singular optical behavior has not been explored or investigated. The remarkable low-loss performance benefits from blue-shifted interband transitions as well as minimal FCA due to strong Anderson localization, substantiated through coupled first-principle modeling and experimental characterization. Record low losses in nonvolatile photonic circuits and electrical pixelated switching were also demonstrated capitalizing on the extraordinary optical properties of this new O-PCM.

Density functional theory (DFT) modeling

We use DFT computations to predict the phase and electronic structures of alloys in the GSST family and reveal promising trends arising from Se substitution. More specifically, we have investigated the Ge₂Sb₂Se_xTe_{5-x} ($x = 0$ to 5) system, the Se-substituted counterparts of the archetypal phase change alloy Ge₂Sb₂Te₅ (GST-225). It is generally expected that substitution of

Te by the lighter Se atoms leads to increased bandgap and hence lessened optical loss in the near-infrared, but the loss decrease has to be traded off with undesirable traits such as reduced optical contrast. The objective of the DFT model, therefore, is to identify the optimal stoichiometry in the $\text{Ge}_2\text{Sb}_2\text{Se}_x\text{Te}_{5-x}$ family for O-PCM applications.



We start by constructing atomic models of the $\text{Ge}_2\text{Sb}_2\text{Se}_x\text{Te}_{5-x}$ alloys (Figs. 1a-c) following procedures detailed in Supplementary Section I, and investigate the basic phase transition behavior of GSST alloys. As shown in Fig. 1d, the cohesive energy difference between the hexagonal and cubic phases is barely affected by Se substitution for Te, hinting a cubic to hexagonal transition path in GSST resembling that of GST-225. Similar to GST-225 whose rapid phase change kinetics necessitates a non-diffusion-controlled process^{41,42}, phase transition in GSST is also associated with a combination of atom block movement and local distortion. However, atomic block

movement in GSST is more difficult to occur compared to GST-225 due to the presence of relatively strong Te-Se bonds at the interfacial layers (bond energies of Te-Te, Te-Se, Se-Se, and Se-Ge are 33.0, 40.6, 44.0, and 49.0 kcal/mol, respectively⁴³). When sufficiently high temperature for Te-Se bond dissociation is reached to unlock atomic block motion, the Te-Te bonds have already broken, likely accompanied by substantial surface reconstruction. Such atomic arrangement perturbation suppresses sliding along the weakly bound Te/Se-Te/Se double layer and formation of vacancy layers essential to the transition towards the metastable cubic phase. Consequently, the temperature window for the metastable phase formation is expected to decrease with increasing Se substitution.

Unlike the cubic phase, the orthorhombic phase's relative stability substantially increases with Se concentration when $x \geq 3$. For GST-225, the orthorhombic phase introduces under-coordinated atoms at the interstitial sites and is energetically unfavorable. At low Se concentration, the Se atoms substitute 6-fold coordinated Te atoms with little impact on the relative stability of the orthorhombic phase. When $x \geq 3$, Se atoms start to fill the interstitial sites with more Se-Ge/Sb bonds formed within the orthorhombic phase than in the hexagonal phase, which stabilizes the orthorhombic phase. The orthorhombic structure is further stabilized at full Se substitution owing to the partial release of geometric restriction imposed by the Te atoms and the consequential reduction of Se-Ge/Sb bond lengths. In addition, pinning by Se-Ge bonds at the interstitial sites impedes atomic block motion, pointing to slow crystallization kinetics in $\text{Ge}_2\text{Sb}_2\text{Se}_5$.

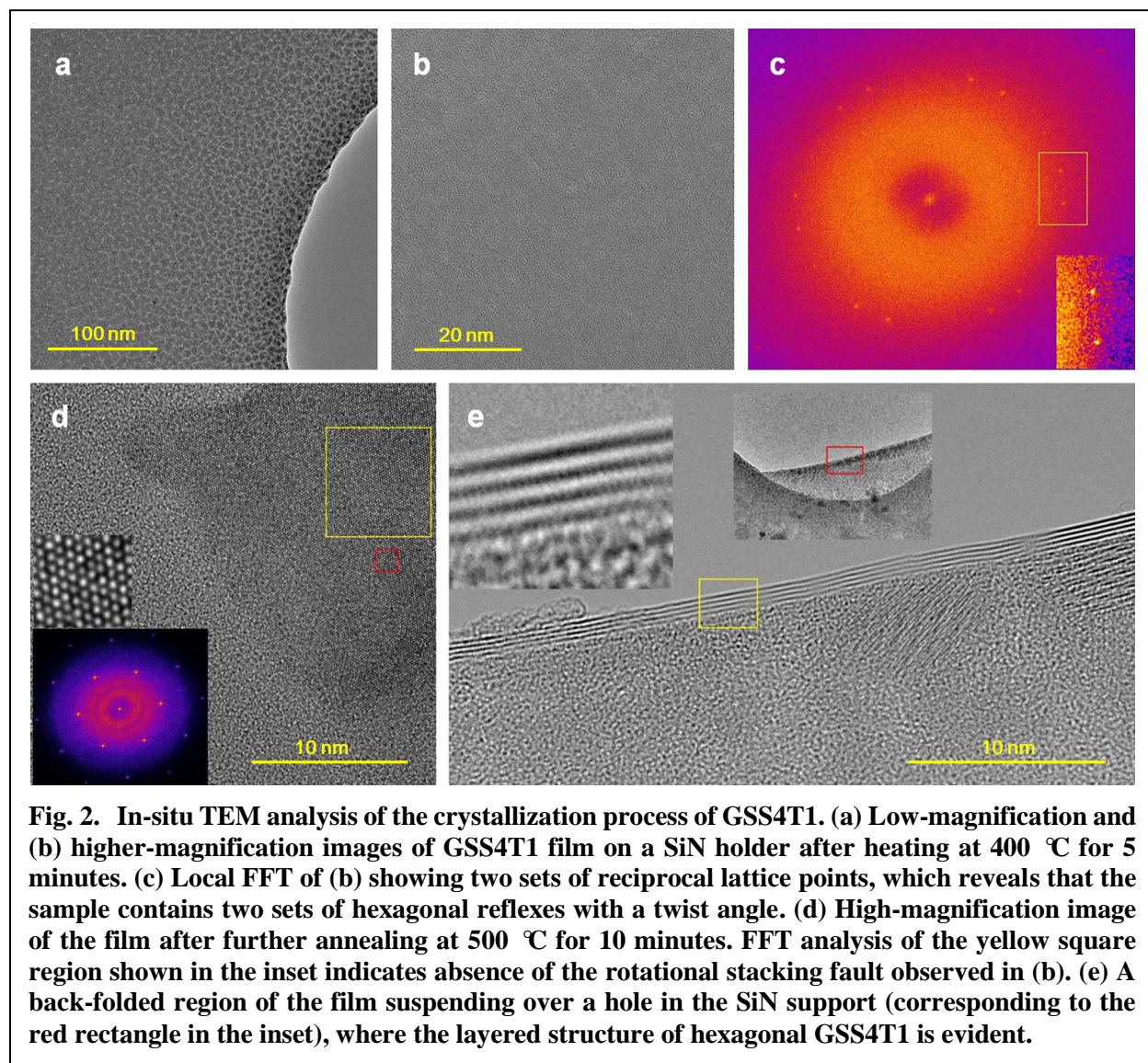
To evaluate the impact on optical properties of Se substitution, we further simulate the electronic band structure of the composition group. Electronic structures modeled by DFT (Fig. 1e) confirm the semiconductor nature of all GSST alloys. The electronic structure is preserved except in $\text{Ge}_2\text{Sb}_2\text{Se}_5$ (Figs. 1f and 1g, Supplementary Section II). The band gap increases with Se addition from 0.1 eV for GST-225 to 0.3 eV for GSS4T1, suggesting a reduction of optical loss in the near-infrared. The DOS peaks are also weakened with increasing Se concentration, contributing to additional absorption suppression. For the orthorhombic $\text{Ge}_2\text{Sb}_2\text{Se}_5$, the theory predicts very weak absorption given its larger bandgap (0.6 eV) than that of the hexagonal phase (0.3 eV). This is expected from stronger quantum confinement induced by 1-D rather than 2-D atomic blocks, an effect visualized through the wavefunction distributions illustrated in Figs. 1h and 1k. Figures 1j and 1k further reveal that misalignment between *p*-orbitals due to the surface curvature of atomic blocks and large amount of interstitial sites in the orthorhombic $\text{Ge}_2\text{Sb}_2\text{Se}_5$ phase eliminates the resonance bonding mechanism. Since resonant bonding has been associated with the large optical contrast of O-PCMs^{44,45}, significantly diminished optical contrast is inferred for $\text{Ge}_2\text{Sb}_2\text{Se}_5$.

In summary, the DFT model suggests $\text{Ge}_2\text{Sb}_2\text{Se}_4\text{Te}_1$ (GSS4T1) as the optimal O-PCM among the compositions investigated. GSS4T1 inherits the resonant bonding mechanism essential for large Δn and the fast, non-diffusion-controlled transition path characteristic of GST-225. The alloy also benefits from reduced interband optical absorption and improved amorphous phase stability. On the other hand, despite its low optical loss, the structurally distinct $\text{Ge}_2\text{Sb}_2\text{Se}_5$ is limited by its severely impeded crystallization kinetics and diminished optical contrast. These theoretical insights are validated by experimental results elaborated in the following section. The DFT model, however, does not account for free carrier effects and are complemented by critical experimental studies of the materials' carrier transport and optical properties detailed below.

Structural, electronic and optical properties of GSST alloys

In order to experimentally confirm and understand the crystal structure of the various GSST compositions, a series of $\text{Ge}_2\text{Sb}_2\text{Se}_x\text{Te}_{5-x}$ ($x = 0$ to 5) films were prepared. Figure S7 in

Supplementary Section III present X-ray diffraction (XRD) spectra of the films annealed at different temperatures. All as-deposited films are amorphous. For films with $x = 0$ to 4, annealing induces a nucleation-dominated phase change where the films first crystallize into a metastable phase followed by complete transition to the stable hexagonal structure. The crystallization onset temperature progressively increases with Se substitution, signaling enhanced amorphous phase stability. The intermediate temperature regime for the metastable phase also diminishes with increasing Se substitution. On the other hand, $\text{Ge}_2\text{Sb}_2\text{Se}_5$ undergoes a sluggish growth-dominated transformation into an orthorhombic equilibrium phase confirmed with selected area electron diffraction (SAED) measurement (Supplementary Section IV). These findings are in excellent agreement with our theoretical predictions. The DFT modeled structures are further corroborated by quantitative fitting of the XRD spectra. For instance, DFT predicts lattice constants of $a = 4.04 \text{ \AA}$ and $c = 16.08 \text{ \AA}$ for hexagonal GSS4T1 whereas XRD fitting yields $a = 4.08 \text{ \AA}$ and $c = 16.08 \text{ \AA}$. Such agreement is satisfactory considering that tensile strains in the order of 1% have been measured in thermally crystallized O-PCM films^{46,47}.



The phase transition process of GSS4T1 was further investigated *in-situ* using aberration-corrected TEM. The as-deposited film was amorphous without visible lattice structure. Figure 2a shows a low-magnification image of GSS4T1 film on a silicon nitride (SiN) holder after heating at a nominal temperature of 400 °C for 5 minutes. Granular contrast is observed, and the higher-magnification TEM image (Fig. 2b) shows lattice structure detectable by a fast Fourier transform (FFT) analysis. The FFT in Fig. 2c reveals that the sample has two sets of hexagonal reflexes with a twist angle between them, indicating a rotation stacking fault between two crystals. We measured the local FFT around different regions in Fig. 2b, and all showed the same pattern suggesting that the rotational twist occurs in the out-of-plane z -direction and not as lateral grains. This means that GSS4T1 forms a layered compound with an initial orientation mismatch between vertically stacked layers. The feature was seen across many regions of the sample.

The temperature was subsequently raised to 500 °C for 10 minutes before cooling down to stop further transformation during TEM examination. Figure 2d shows a high-magnification image of a well-crystallized area with strong lattice contrast visible. Similar single-crystal patterns were observed across the entire sample in FFT, signifying that the rotational misorientation present at 400 °C has been removed by high temperature annealing. We also located a region where the film was suspended over a hole in the SiN support and had back folded (Fig. 2e). The back-folded region shows multiple lines of contrast in its profile similar to back-folded layered 2-D materials⁴⁸, affirming the layered structure of hexagonal GSS4T1.

The observed layered structure is consonant with the DFT model depicted in Fig. 1a. The rotational stacking fault most likely occurs at the Se-Te double layer where the bonding is weak and many high-symmetry interfacial configurations exist as local energy minima (Supplementary Section V). At elevated temperatures, thermal fluctuation enables the system to explore a large range of configurational space, and eventually drives it towards the global minimum, i.e. a single-crystal-like structure.

In order to experimentally verify the reduction in FCA with Se substitution, both electronic and optical measurements were performed. Electronic transport properties of the GSST alloys were studied using Hall measurement. *In-situ* conductivity measurement during annealing (Fig. 3a) indicates that the electrical resistivity of GSST sharply drops coinciding with occurrence of phase transitions, followed by continuous decrease as annealing temperature rises due to vacancy ordering⁴⁹. Room-temperature resistivity of GSS4T1 is over two orders of magnitude larger compared to that of GST (Fig. 3b). For all compositions, the crystalline materials show p-type conduction similar to that of the prototypical GST-225 alloy⁵⁰ with relatively minor change in Hall carrier concentrations (Fig. 3c). The drastic resistivity increase with Se substitution is therefore mostly attributed to the reduction of free carrier mobility due to Anderson localization (Fig. 3d). This is consistent with the negligible energy penalties associated with structural perturbations within the Te/Se double layer predicted by our DFT simulations (Fig. S3), which results in pronounced atomic disorder and decoupling of directional p -bonds. Unlike GST-225, c-GSS4T1 consistently exhibits negative temperature coefficients of resistivity regardless of annealing temperature (Fig. 3e), signaling non-metallic behavior of c-GSS4T1 (Supplementary Section VI)²⁴.

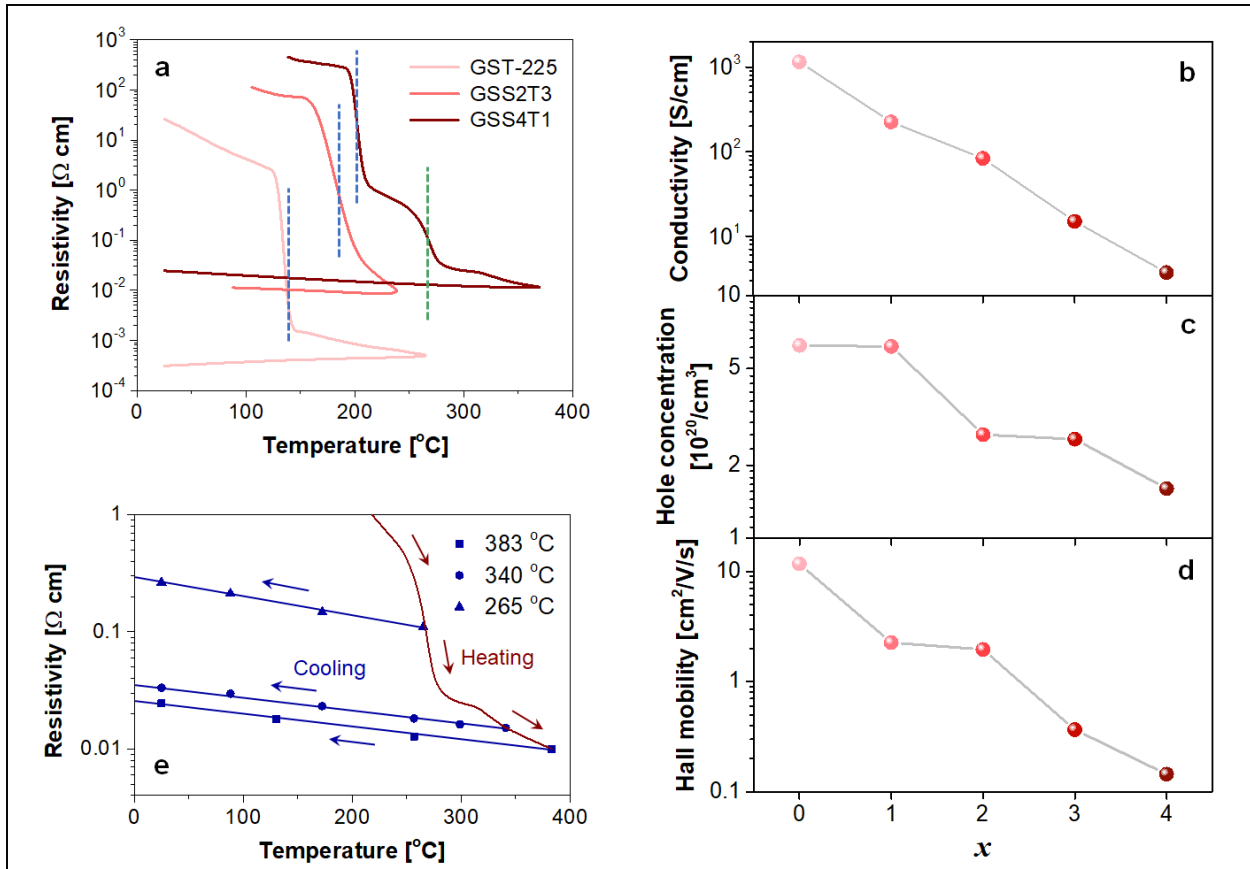


Fig. 3. Electronic properties of $\text{Ge}_2\text{Sb}_2\text{Se}_x\text{Te}_{5-x}$ alloys. (a) Temperature dependence of resistivity of $\text{Ge}_2\text{Sb}_2\text{Te}_5$, $\text{Ge}_2\text{Sb}_2\text{Se}_2\text{Te}_3$, and $\text{Ge}_2\text{Sb}_2\text{Se}_4\text{Te}_1$ upon annealing: the distinct drop marked by blue dotted lines correspond to crystallization of the amorphous phase to the metastable cubic phase, whereas the green dotted line labels the transition towards the stable hexagonal phase. (b) Hall conductivity, (c) hole concentration, and (d) Hall mobility of $c\text{-Ge}_2\text{Sb}_2\text{Se}_x\text{Te}_{5-x}$; for all compositions, the films were annealed 50 $^\circ\text{C}$ above the amorphous-to-cubic transition temperature. (e) Temperature-dependent resistivity of $\text{Ge}_2\text{Sb}_2\text{Se}_4\text{Te}_1$ annealed at different three temperatures: 265 $^\circ\text{C}$, 340 $^\circ\text{C}$, and 383 $^\circ\text{C}$. The temperature coefficients of resistivity are negative in all cases evidenced by the negative slope of the cooling curves.

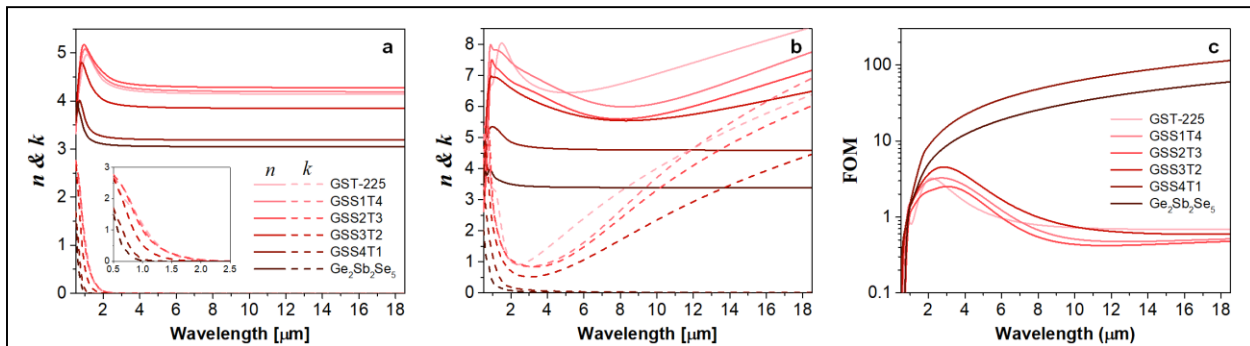
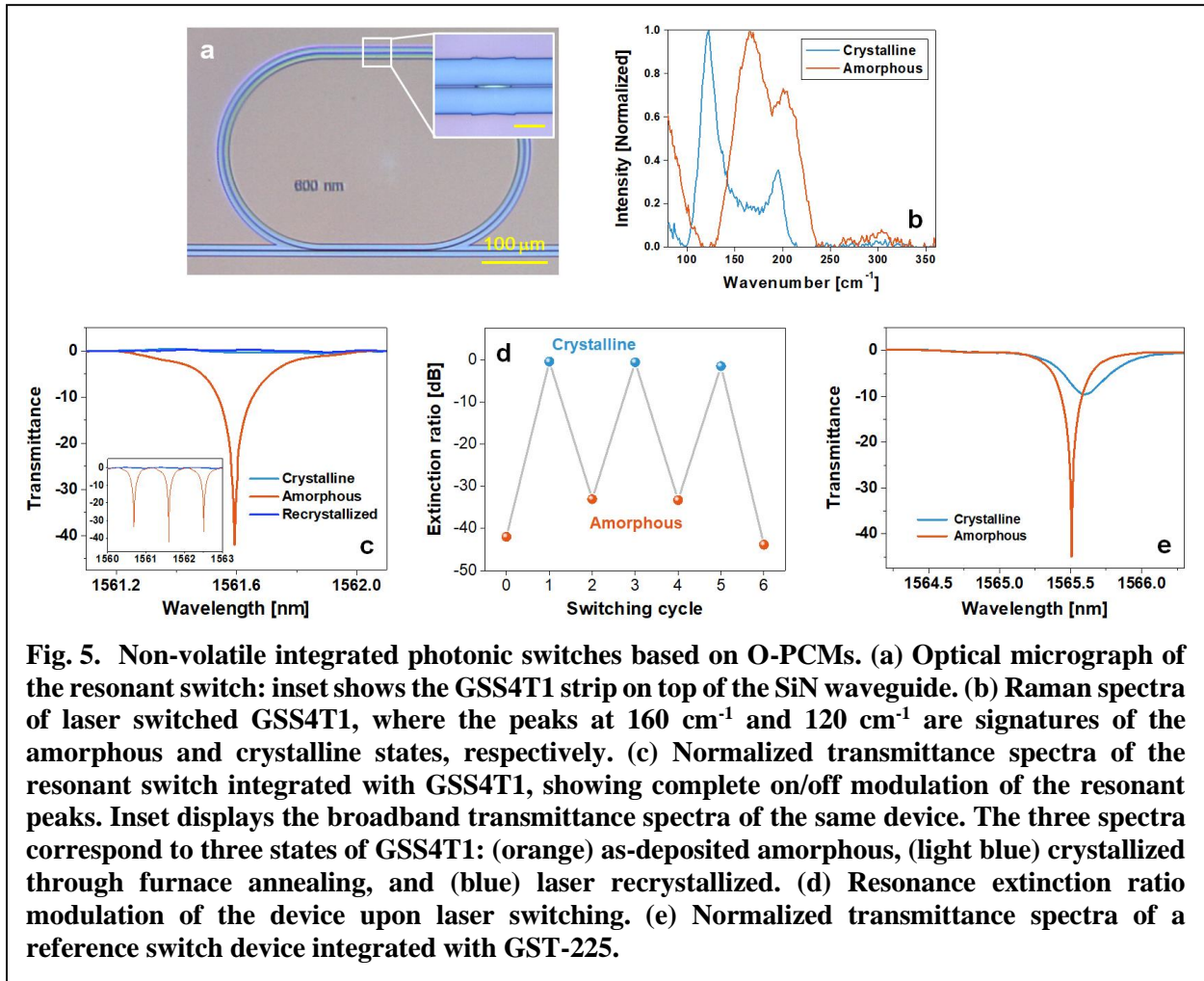


Fig. 4. Optical properties of $\text{Ge}_2\text{Sb}_2\text{Se}_x\text{Te}_{5-x}$ films. (a, b) Measured real (n) and imaginary (k) parts of refractive indices of the (a) amorphous and (b) crystalline alloys. (c) Material FOM's.

While such elevated resistivity is critical to suppressing FCA, the fact that c-GSS4T1 behaves as an Anderson insulator raises the question of whether large optical property contrast, the hallmark of O-PCMs, can be maintained in the absence of an MIT. To address this question, the Kramers-Kronig consistent optical constants of GSST alloys were obtained using coupled spectroscopic ellipsometry and transmittance/reflectance measurements from the visible through long-wave infrared (Figs. 4a and 4b). GSS4T1 exhibits a large Δn of 2.1 to 1.7 across the near- to mid-IR bands, suggesting that MIT is not a prerequisite for O-PCMs. Moreover, its remarkably broad transparency window (1 – 18.5 μm) owing to blue-shifted band edge and minimal FCA yields a FOM two orders of magnitude larger than those of GST and other GSST compositions (Fig. 4c). While $\text{Ge}_2\text{Sb}_2\text{Se}_5$ similarly exhibits broadband optical transparency, its FOM is inferior to that of GSS4T1 due to its low index contrast. The experimentally confirmed FOM benefit of the optimized GSS4T1 composition validates the successful prediction of the DFT simulations.

High-performance nonvolatile integrated photonic switch demonstration



Integrated optical switches are essential components of photonic integrated circuits. Traditional optical switches mostly operate on miniscule electro-optic or thermo-optic effects, thereby demanding long device lengths. The large index contrast furnished by O-PCMs potentially allows drastic size down scaling of these devices. However, at the 1550 nm telecommunication

wavelength, GST-225 and VO₂ exhibit low FOM's of 2.0 and 0.4, respectively. Consequently, optical switches experimentally realized based on these materials only provide moderate contrast ratio (CR) and insertion loss (IL) of 12 dB and -2.5 dB⁵⁻⁹. Compounded parasitic losses and crosstalk preclude scalable integration of these individual devices to form large-scale, functional photonic circuits. Here we exploit the exceptional FOM of GSS4T1 to realize a nonvolatile photonic switch with unprecedented high performance. Figure 5a shows an image of the switch device comprising a SiN racetrack resonator coupled to a bus waveguide. A 50-nm thick strip of GSS4T1 was deposited on the resonator as illustrated in the inset. Phase transition of GSS4T1 was actuated using normal-incident laser pulses and confirmed via Raman spectroscopy. Figures 5b plot the Raman spectra of the GSS4T1 strip in both structural states, where the peaks at 160 cm⁻¹ and 120 cm⁻¹ are signatures of the amorphous and crystalline states, respectively. The optical property change turns on/off resonant transmission through the switch reversibly over multiple cycles, evidenced by the measured transmittance spectra in Fig. 5c and the corresponding extinction ratio modulation (Fig. 5d). The device exhibits a large switching CR of 42 dB and a low IL of < 0.5 dB, far outperforming previous nonvolatile switches⁵⁻⁹ as well as devices based on the classical GST-225 material with a similar configuration (Fig. 5e); as can be seen from Fig. 5d, the resonance peak is not completely turned off even when GST-225 is transformed into the crystalline state. Such remarkable performance is consistent with theoretical predictions based on the measured optical constants of GSS4T1 (Supplementary Section VII) and is attributed to its exceptional FOM.

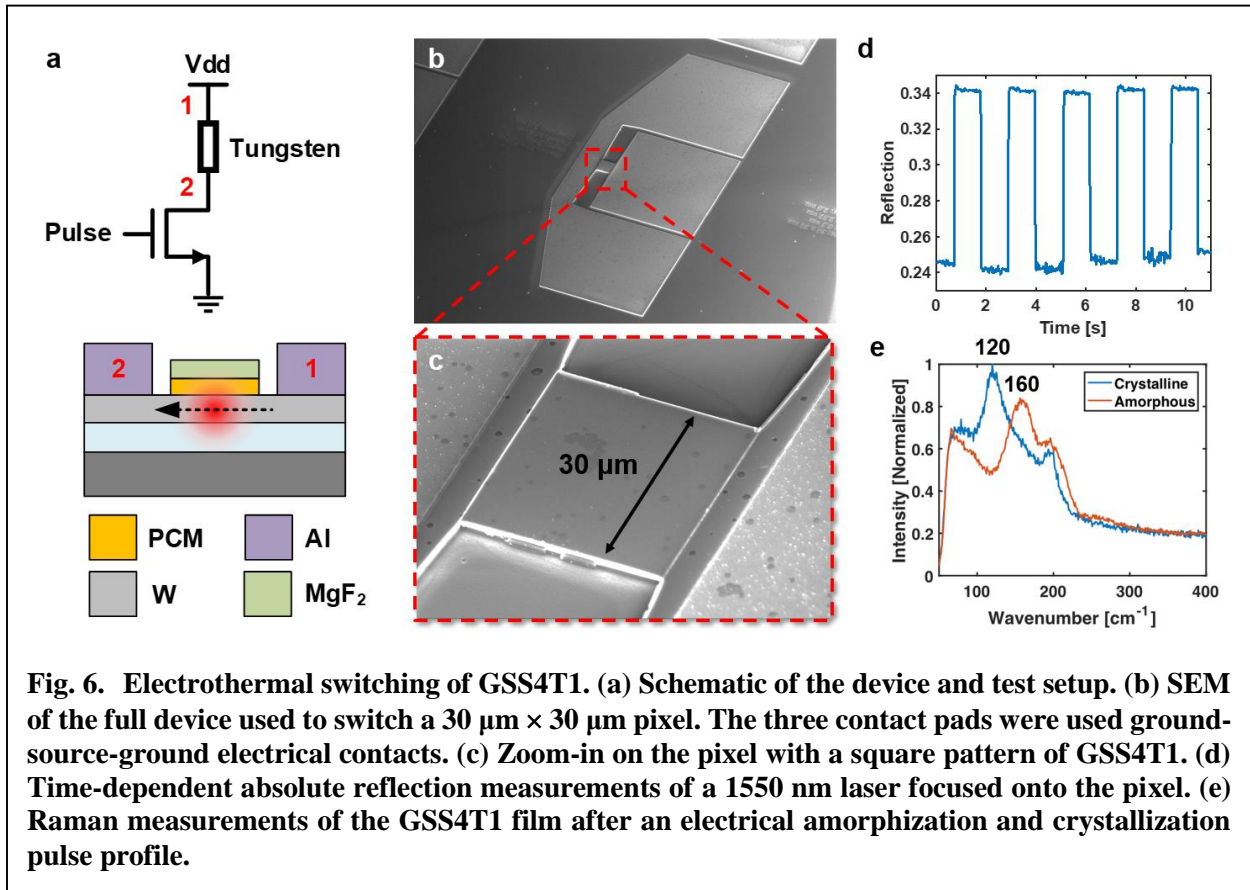
Pixel-level electrothermal switch for free-space reflection modulation

The new O-PCM also enables a broad class of tunable free-space optical devices capable of arbitrary phase or amplitude modulation for agile beam control in the infrared. As a proof-of-concept, we demonstrate reversible electrothermal switching of the GSS4T1 in a reflective pixel device. Heat is applied to the material externally via joule heating of a tungsten metal layer in contact with the GSS4T1, as shown in Fig. 6a. Pulse train profiles are applied to the pixel via the gate of a power MOSFET connected in series to the device. Figure 6b shows the SEM image of a full device with the contact pads and Fig. 6c shows the zoom-in on the GSS4T1 patterned pixel. To monitor the state of the material, a 1550 nm laser was focused onto the pixel and the reflection was recorded on an InGaAs video camera with a frame rate of 100 fps. The time dependent reflection measurement, shown in Fig. 6d, demonstrates an absolute reflection change from 24% to 34%, which corresponds to a relative change in reflection of 41%. The contrast can be further improved with an optimized multilayer film stack design and our simulations predict that up to 30 dB contrast can be achieved in the short-wave infrared range. Raman measurement of the material structure confirms the electrically switched crystalline and amorphous peaks at 120 cm⁻¹ and 160 cm⁻¹, respectively, as shown in Fig. 6e. The device has been demonstrated to switch over 1,000 cycles, as discussed in Supplementary Section VIII.

Conclusion

In this article, we demonstrated a new class of O-PCMs GSST engineered to achieve index-only modulation free from the loss penalty. Guided by first-principle computational designs, the compositionally optimized alloy Ge₂Sb₂Se₄Te₁ claims an unprecedented material FOM over two orders of magnitude larger than that of classical GST alloys, benefiting from blue-shifted interband transitions as well as minimal FCA. A nonvolatile optical switch was realized based on Ge₂Sb₂Se₄Te₁. Its record low loss and switching contrast, derived from the exceptional FOM of the material, qualify the device as a useful building block for scalable photonic networks. An

electrothermally switched free-space reflective pixel was also demonstrated with a microsecond amorphization switching time and relative contrast of 41% at 1550 nm. These results enable a new path for electrical free-space infrared light control for applications in spatial light modulators, tunable reflective spectral filters, subwavelength reflective phased arrays, beam steering, holography, and tunable metasurfaces. Moreover, isoelectronic substitution with light elements, as illustrated in our example of GSST, points to a generic route in the search of new O-PCMs optimized for future photonic applications.



Methods

DFT modeling. Standard ab-initio calculations within the framework of density-functional theory were performed using the Vienna Ab Initio Simulation Package (VASP v5.4)⁵¹. Plane-wave and projector-augmented-wave (PAW)⁵² type pseudopotentials were applied with the electronic configurations of Ge: $4s^24p^2$, Sb: $5s^25p^3$, Te: $5s^25p^4$, Se: $4s^24p^4$, and a 300 eV kinetic-energy cutoff. Exchange-correlation effects were described with the GGA-PBESol functional⁵³. The structures were relaxed until all forces were smaller than 0.01 eV/Å. K-point grids of $12 \times 12 \times 4$, $12 \times 12 \times 1$, and $2 \times 9 \times 2$ were used for geometric optimization in hexagonal, cubic, and orthorhombic phases, while those for the electronic structure calculations are $24 \times 24 \times 8$, $24 \times 24 \times 2$, and $4 \times 18 \times 4$, respectively. The tetrahedron method with Blöchl corrections were employed to obtain total energies. While the cohesive energy strongly depends on the exchange-correlation functional employed in DFT, the relative energy differences between various phases and sequences are much less sensitive, enabling the comparison of stability between various configurations in this work – a method similarly adopted in previous studies⁴¹. Since the entropy contributions to the free energies have not been accounted in this work, and the standard DFT calculations only provide solutions at 0 K, our results cannot predict the driving force for transition between different structures accurately. Nevertheless, the variations of cohesive energy obtained with our approach are sufficient to qualitatively reveal the impact of Se substitution within each phase.

Material synthesis. Thin films of GSST were prepared using thermal evaporation from a single $\text{Ge}_2\text{Sb}_2\text{Se}_4\text{Te}_1$ source. Bulk starting material of $\text{Ge}_2\text{Sb}_2\text{Se}_4\text{Te}_1$ was synthesized using a standard melt quench technique from high-purity (99.999%) raw elements⁵⁴. The film deposition was performed using a custom-designed system (PVD Products, Inc.) following previously established protocols⁵⁵. The substrate was not actively cooled, although the substrate temperature was measured by a thermocouple and maintained at below 40 °C throughout the deposition process. Stoichiometries of the films were confirmed using wavelength-dispersive spectroscopy (WDS) on a JEOL JXA-8200 SuperProbe Electron Probe Microanalyzer (EPMA) to be within 2% (atomic fraction) deviation from target compositions.

Material characterizations. Grazing incidence X-Ray diffraction (GIXRD) was performed using a Rigaku Smartlab Multipurpose Diffractometer (Cu $K\alpha$ radiation) equipped with a high-flux 9 kW rotating anode X-ray source, parabolic graded multilayer optics and a scintillation detector. The GIXRD patterns were collected within one hour over a range of $2\theta = 10 - 80$ degrees at room temperature.

Prior to electrical conductivity and Hall measurement, Ti/Au (10/100 nm thickness) contacts were deposited using electron beam evaporation through a shadow mask. A 3-nm thick layer of alumina were then deposited on top of the GSST film as capping layer using atomic layer deposition to prevent film vaporization and surface oxidation. Hall and electrical conductivity measurements were carried out on a home-built Van der Pauw testing station. The samples were heat treated using a hotplate.

Optical properties of the films were measured with NIR ellipsometry from 500 nm – 2,500 nm wavelengths in combination with a reflection and transmission Fourier transform infrared (FTIR) spectroscopy measurement from 2,500 nm – 18,500 nm wavelengths. A gold mirror was used as the reference for the reflection measurement. Fitting of the real and imaginary parts of the refractive indices was performed with the Woollam WVASE software. The method allows us to quantify the material's imaginary part of refractive index down to below 0.01.

In-situ TEM analysis. The sample was prepared on thin silicon nitride membranes with 2-micron holes, on which a 10 nm thick GSS4T1 film was deposited. Imaging was performed using Oxford's JEOL 2200 MCO aberration-corrected transmission electron microscope with CEOS (Corrected Electron Optical Systems GmbH) image corrector and an accelerating voltage of 80 kV. A heating holder (DENSolutions) was used for *in-situ* temperature control. All temperatures quoted in the manuscript regarding the TEM analysis are nominal values as given by the heating holder control, which can be slightly different from temperature of the sample on the SiN membrane due to thermal non-uniformity.

Device fabrication. The resonator devices and electrothermal switching devices were fabricated on silicon wafers with 3 μm thermal oxide from Silicon Quest International. To fabricate the resonator devices, 400 nm SiN was first deposited using low pressure chemical vapor deposition. The resonators were patterned using electron beam lithography on an Elionix ELS-F125 electron-beam lithography (EBL) system followed by reactive ion etching (CHF_3/CF_4 etching gas with 3:1 ratio at 30 mTorr total pressure). A 50-nm layer of GSS4T1 were then deposited and patterned using poly(methyl methacrylate) (PMMA) as the lift-off resist and subsequently capped with 20 nm of SiO_2 deposited using plasma-enhanced chemical vapor deposition (PECVD). The electrothermal switching devices were fabricated from a 50-nm thick, evaporated tungsten film. Patterning of tungsten was achieved via reactive ion etching. 200-nm-thick aluminum contact pads were evaporated and patterned via lift off. 50 nm of GSS4T1 was then deposited, patterned via liftoff, and encapsulated in 20 nm evaporated MgF_2 .

Integrated photonic device characterization. The optical switch devices were measured on a home-built grating coupling system used in conjunction with an external cavity tunable laser (Luna Technologies) with a built-in optical vector analyzer. Laser light was coupled into and out of the devices using single-fiber probes. Details of the characterization setup can be found elsewhere⁵⁶. The devices under test (DUT) were maintained at room temperature throughout the measurement.

Laser-induced phase transition. The laser system used to optically switch the phase change films consisted of a 633 nm and a 780 nm continuous-wave laser with a total optical power of 136 mW. An acoustic optical modulator with a 2 ns rise time was used to modulate the laser output to generate optical pulse trains. For amorphous to crystallization phase transitions, a pulse train with period of 1 μs , duty cycle of 0.03% (30 ns), and 100,000 repetitions was used. For crystalline to amorphous phase transitions, a single pulse with a width of 100 ns was used.

Electrothermal switching. In order to electrically amorphize GSS4T1, a single 1 μs pulse at 24 V is applied with a switching energy of 5.5 μJ . For crystallization, a pulse train consisting of 50 pulses with a period of 1 ms and duty cycle of 50% at 13 V is applied with a total switching energy of 42.5 mJ. Here the switching energy figures are quoted for 30 μm \times 30 μm pixels, and we also experimentally demonstrated that the switching power can be reduced with smaller pixel sizes (Supplementary Section IX).

Acknowledgements

The authors would like to thank Jeffrey Grossman for helpful discussions and support to this work, and Skylar Deckoff-Jones for assistance with measurements. This material is based upon work supported by the Assistant Secretary of Defense for Research and Engineering under Air Force Contract No. FA8721-05-C-0002 and/or FA8702-15-D-0001, and by the Defense Advanced Research Projects Agency Defense Sciences Office (DSO) Program: EXTREME Optics and Imaging (EXTREME) under Agreement No. HR00111720029. The authors also acknowledge characterization facility support provided by the Materials Research Laboratory at MIT, as well as fabrication facility support by the Microsystems Technology Laboratories at MIT and Harvard University Center for Nanoscale Systems. The views, opinions and/or findings expressed are those of the authors and should not be interpreted as representing the official views or policies of the Department of Defense or the U.S. Government. H.L. also acknowledges the support from the National Natural Science Foundation of China (11804403) and the Natural Science Foundation of Guangdong Province (2018B030306036). This research used computational resources of the National Supercomputer Center in Guangzhou.

Author contributions

Y.Z. deposited and characterized the material, modeled and fabricated the devices, and performed device measurement. J.B.C. and V.L. developed the laser and electrothermal switching method, performed thin film optical property characterizations, and helped with device design and fabrication. J.L. first developed the materials and device integration protocols. H. Li carried out the DFT modeling and interpreted the results. Q.D. conducted thin film structural analysis and assisted in device processing and testing. A.Y. and M.K. synthesized the bulk materials for thin film deposition. S.Z. and J.W. carried out the *in-situ* TEM

imaging and data analysis. Z.F., M.Y.S., C. Roberts, C. R ós, and P.R. contributed to device fabrication. H.Z., B.B., H. Lin and T.G. assisted in device measurement and data analysis. J.L. and J.H. conceived the project. J.W., V.L., K.R., and J.H. supervised the research. All authors contributed to technical discussions and writing the paper.

Competing financial interests

The authors declare no competing financial interests.

References

- 1 Shi, J., Zhou, Y. & Ramanathan, S. Colossal resistance switching and band gap modulation in a perovskite nickelate by electron doping. *Nature Communications* **5**, 4860 (2014).
- 2 Lu, N. *et al.* Electric-field control of tri-state phase transformation with a selective dual-ion switch. *Nature* **546**, 124-128 (2017).
- 3 Wuttig, M., Bhaskaran, H. & Taubner, T. Phase-change materials for non-volatile photonic applications. *Nature Photonics* **11**, 465-476, doi:10.1038/nphoton.2017.126 (2017).
- 4 Waldecker, L. *et al.* Time-domain separation of optical properties from structural transitions in resonantly bonded materials. *Nature Materials* **14**, 991 (2015).
- 5 Stegmaier, M., Ríos, C., Bhaskaran, H., Wright, C. D. & Pernice, W. H. Nonvolatile All-Optical 1 × 2 Switch for Chipscale Photonic Networks. *Advanced Optical Materials* **5**, 1600346 (2017).
- 6 Rudé M. *et al.* Optical switching at 1.55 μm in silicon racetrack resonators using phase change materials. *Appl. Phys. Lett.* **103**, 141119 (2013).
- 7 Moriyama, T. *et al.* Ultra-compact, self-holding asymmetric Mach-Zehnder interferometer switch using $\text{Ge}_2\text{Sb}_2\text{Te}_5$ phase-change material. *IEICE Electronics Express* **11**, 20140538-20140538 (2014).
- 8 Kato, K., Kuwahara, M., Kawashima, H., Tsuruoka, T. & Tsuda, H. Current-driven phase-change optical gate switch using indium-tin-oxide heater. *Applied Physics Express* **10**, 072201 (2017).
- 9 Tanaka, D. *et al.* Ultra-small, self-holding, optical gate switch using $\text{Ge}_2\text{Sb}_2\text{Te}_5$ with a multi-mode Si waveguide. *Opt. Express* **20**, 10283-10294 (2012).
- 10 Zhang, Q. *et al.* Broadband nonvolatile photonic switching based on optical phase change materials: beyond the classical figure-of-merit. *Opt. Lett.* **43**, 94-97, doi:10.1364/OL.43.000094 (2018).
- 11 Hosseini, P., Wright, C. D. & Bhaskaran, H. An optoelectronic framework enabled by low-dimensional phase-change films. *Nature* **511**, 206-211 (2014).
- 12 Gholipour, B., Zhang, J., MacDonald, K. F., Hewak, D. W. & Zheludev, N. I. An all-optical, non-volatile, bidirectional, phase-change meta-switch. *Adv. Mater.* **25**, 3050-3054 (2013).
- 13 Wang, Q. *et al.* Optically reconfigurable metasurfaces and photonic devices based on phase change materials. *Nature Photonics* **10**, 60-65, doi:10.1038/Nphoton.2015.247 (2016).
- 14 Yin, X. *et al.* Beam switching and bifocal zoom lensing using active plasmonic metasurfaces. *Light: Science & Applications* **6**, e17016 (2017).
- 15 de Galarreta, C. R. *et al.* Nonvolatile Reconfigurable Phase-Change Metadevices for Beam Steering in the Near Infrared. *Adv. Funct. Mater.* (2018).
- 16 Dong, W. *et al.* Tunable Mid-Infrared Phase-Change Metasurface. *Advanced Optical Materials* **6**, 1701346, doi:doi:10.1002/adom.201701346 (2018).
- 17 Rudé M. *et al.* Ultrafast and Broadband Tuning of Resonant Optical Nanostructures Using Phase-Change Materials. *Advanced Optical Materials* **4**, 1060-1066, doi:10.1002/adom.201600079 (2016).
- 18 Tittl, A. *et al.* A switchable mid-infrared plasmonic perfect absorber with multispectral thermal imaging capability. *Adv. Mater.* **27**, 4597-4603 (2015).
- 19 Du, K.-k. *et al.* Control over emissivity of zero-static-power thermal emitters based on phase-changing material GST. *Light: Science and Applications* **6**, e16194 (2017).
- 20 Michel, A.-K. U. *et al.* Using Low-Loss Phase-Change Materials for Mid-Infrared Antenna Resonance Tuning. *Nano Letters* **13**, 3470-3475, doi:10.1021/nl4006194 (2013).
- 21 Ríos, C. *et al.* Integrated all-photonic non-volatile multi-level memory. *Nature Photonics* **9**, 725-732 (2015).

- 22 Rios, C., Hosseini, P., Wright, C. D., Bhaskaran, H. & Pernice, W. H. On-Chip Photonic Memory Elements Employing Phase-Change Materials. *Adv. Mater.* **26**, 1372-1377 (2014).
- 23 Feldmann, J. *et al.* Calculating with light using a chip-scale all-optical abacus. *Nature Communications* **8**, 1256 (2017).
- 24 Siegrist, T. *et al.* Disorder-induced localization in crystalline phase-change materials. *Nature Materials* **10**, 202 (2011).
- 25 Reed, G. T., Mashanovich, G., Gardes, F. Y. & Thomson, D. J. Silicon optical modulators. *Nature Photonics* **4**, 518, doi:10.1038/nphoton.2010.179 (2010).
- 26 Yu, Z. *et al.* Enhancing far-field thermal emission with thermal extraction. *Nature Communications* **4**, 1730 (2013).
- 27 Ono, M., Chen, K., Li, W. & Fan, S. Self-adaptive radiative cooling based on phase change materials. *Optics Express* **26**, A777-A787, doi:10.1364/OE.26.00A777 (2018).
- 28 Zhang, Z., You, Z. & Chu, D. Fundamentals of phase-only liquid crystal on silicon (LCOS) devices. *Light: Science & Applications* **3**, e213, doi:10.1038/lsa.2014.94 (2014).
- 29 Shen, Y. *et al.* Deep learning with coherent nanophotonic circuits. *Nature Photonics* **11**, 441 (2017).
- 30 Soref, R. A., McDaniel, D. & Bennett, B. R. Guided-wave intensity modulators using amplitude-and-phase perturbations. *J. Lightwave Technol.* **6**, 437-444 (1988).
- 31 Sun, X. Y. *et al.* Single-step deposition of cerium-substituted yttrium iron garnet for monolithic on-chip optical isolation. *ACS Photonics* **2**, 856-863 (2015).
- 32 Nedeljkovic, M., Soref, R. & Mashanovich, G. Z. Predictions of free-carrier electroabsorption and electrorefraction in germanium. *IEEE Photonics Journal* **7**, 1-14 (2015).
- 33 Astill, A. Material figures of merit for non-linear optics. *Thin Solid Films* **204**, 1-17 (1991).
- 34 Adam, J.-L. & Zhang, X. *Chalcogenide glasses: preparation, properties and applications.* (Woodhead publishing, 2014).
- 35 Lyeo, H.-K. *et al.* Thermal conductivity of phase-change material Ge₂Sb₂Te₅. *Appl. Phys. Lett.* **89**, 151904, doi:10.1063/1.2359354 (2006).
- 36 Svoboda, R. & Málek, J. Amorphous-to-crystalline transition in Te-doped Ge₂Sb₂Se₅ glass. *J. Therm. Anal. Calorim.* **117**, 1073-1083 (2014).
- 37 Vinod, E., Ramesh, K. & Sangunni, K. Structural transition and enhanced phase transition properties of Se doped Ge₂Sb₂Te₅ alloys. *Scientific Reports* **5**, 8050 (2015).
- 38 Buller, S. *et al.* Influence of partial substitution of Te by Se and Ge by Sn on the properties of the Blu-ray phase-change material Ge₈Sb₂Te₁₁. *Chem. Mater.* **24**, 3582-3590 (2012).
- 39 Koch, C. *et al.* Investigating the Influence of Resonant Bonding on the Optical Properties of Phase Change Materials (GeTe)_xSnSb₂Se₄. *Chem. Mater.* **29**, 9320-9327 (2017).
- 40 Koch, C. *et al.* Enhanced temperature stability and exceptionally high electrical contrast of selenium substituted Ge₂Sb₂Te₅ phase change materials. *RSC Advances* **7**, 17164-17172 (2017).
- 41 Sun, Z. M., Zhou, J. & Ahuja, R. Structure of phase change materials for data storage. *Physical Review Letters* **96**, doi:10.1103/PhysRevLett.96.055507 (2006).
- 42 Elliott, S. R. Chalcogenide Phase-Change Materials: Past and Future. *International Journal of Applied Glass Science* **6**, 15-18 (2015).
- 43 El-Din, K. S. a. E. A. M. a. F. S. T. a. A. S. a. S. M. Optical properties of amorphous chalcogenide thin films: The effect of Te isovalence substitution in the Ge-S-Se system. *Journal of Physics D: Applied Physics* **27**, 156 (1994).
- 44 Shportko, K. *et al.* Resonant bonding in crystalline phase-change materials. *Nature Materials* **7**, 653-658, doi:10.1038/nmat2226 (2008).
- 45 Welnic, W., Botti, S., Reining, L. & Wuttig, M. Origin of the optical contrast in phase-change materials. *Physical Review Letters* **98**, doi:10.1103/PhysRevLett.98.236403 (2007).
- 46 Nazeer, H., Bhaskaran, H., Woldering, L. A. & Abelmann, L. Young's modulus and residual stress of GeSbTe phase-change thin films. *Thin Solid Films* **592**, 69-75 (2015).

- 47 Pedersen, T. L. *et al.* Mechanical stresses upon crystallization in phase change materials. *Appl. Phys. Lett.* **79**, 3597-3599 (2001).
- 48 Warner, J. H., Rümmeli, M. H., Gemming, T., Bückner, B. & Briggs, G. A. D. Direct Imaging of Rotational Stacking Faults in Few Layer Graphene. *Nano Lett.* **9**, 102-106, doi:10.1021/nl8025949 (2009).
- 49 Zhang, W. *et al.* Role of vacancies in metal–insulator transitions of crystalline phase-change materials. *Nature Materials* **11**, 952 (2012).
- 50 Lee, B.-S. *et al.* Investigation of the optical and electronic properties of Ge₂Sb₂Te₅ phase change material in its amorphous, cubic, and hexagonal phases. *J. Appl. Phys.* **97**, 093509 (2005).
- 51 Kresse, G. & Furthmüller, J. Efficient iterative schemes for ab initio total-energy calculations using a plane-wave basis set. *Physical Review B* **54**, 11169-11186, doi:10.1103/PhysRevB.54.11169 (1996).
- 52 Blochl, P. E. Projector augmented-wave method. *Physical Review B* **50**, 17953-17979, doi:10.1103/PhysRevB.50.17953 (1994).
- 53 Perdew, J. P. *et al.* Restoring the density-gradient expansion for exchange in solids and surfaces. *Physical Review Letters* **100**, doi:10.1103/PhysRevLett.100.136406 (2008).
- 54 Petit, L. *et al.* Compositional dependence of the nonlinear refractive index of new germanium-based chalcogenide glasses. *J. Solid State Chem.* **182**, 2756-2761 (2009).
- 55 Hu, J. *et al.* Fabrication and testing of planar chalcogenide waveguide integrated microfluidic sensor. *Opt. Express* **15**, 2307-2314 (2007).
- 56 Lin, H. *et al.* Chalcogenide glass-on-graphene photonics. *Nature Photonics* **11**, 798-805 (2017).